Supporting information for

Constructing large-size and ultrathin NiCoP nanosheets on Fe₂O₃ photoanode toward efficient solar water splitting

Chenchen Feng,[a] Bin Zhao,[a,b] Yingpu Bi[a]*

[a] State Key Laboratory for Oxo Synthesis & Selective Oxidation, National Engineering Research Center for Fine

Petrochemical Intermediates, Lanzhou Institute of Chemical Physics, CAS, Lanzhou, Gansu 730000, China.

[b] University of Chinese Academy of Sciences, Beijing 100049, China.

Corresponding authors: Yingpu Bi, E-mail: yingpubi@licp.cas.cn

Experimental section

Preparation of Fe$_2$O$_3$ photoanode:

Herein, Fe$_2$O$_3$ nanorod arrays with 3D dendritic structure were grown on the acid treated Ti foils. Firstly, Ti foils (1 cm×5 cm) were cleaned by sonication in acetone, ethanol and deionized water to remove surface impurities, and then treated in hot hydrochloric acid. For the HCl treatment of Ti foils, the cleaned Ti foils were immersed into 30 mL concentrated hydrochloric acid and kept it at 80 °C for 40 min. After that, Ti foils were immediately removed from the hot HCl solution and washed with water for several times. For the hydrothermal growth of FeOOH nanorods, 1.215 g FeCl$_3$·6H$_2$O and 0.27 g urea were dissolved in 60 mL deionized water under vigorous stirring for 30 min. Then the solution was transfer to a Teflon-lined stainless-steel autoclave (80 mL) in which a piece of acid-treated Ti foil was immersed into the solution. Then the autoclave was sealed and maintained at 100 °C for 10 h in an electric oven. After the autoclave cooled down at room temperature naturally, the Ti foil covered with FeOOH nanorods was taken out and washed with water and ethanol for several times, followed by drying at 60 °C. Finally, the precursor film was annealed at 550 °C in air for 2 h to obtain Fe$_2$O$_3$ photoanode.

Preparation of NiCo(OH)$_x$/Fe$_2$O$_3$ and NiCoP/Fe$_2$O$_3$ photoanode:

Firstly, the obtained Fe$_2$O$_3$ nanorods photoanode was immersed in a 100 mL aqueous solution containing 5 mmol Ni(SO$_4$)$_2$·6H$_2$O and 5 mmol Co(SO$_4$)$_2$·7H$_2$O, which was kept at room temperature for 1 h for the growth of the NiCo(OH)$_x$ on the surface of the Fe$_2$O$_3$ nanorods. After this, the sample was taken out, washed with water and dried in 60 °C. For the preparation of NiCoP/Fe$_2$O$_3$, 1.5 g NaH$_2$PO$_2$ was placed at the upstream side of a tube furnace and the NiCo(OH)$_x$/Fe$_2$O$_3$ photoanode was placed at the downstream side. Subsequently, the sample was heated to 350 °C in a stream of Ar gas for 2 h.

Preparation of NiCoO$_x$/Fe$_2$O$_3$ and NiCoP(O)/Fe$_2$O$_3$ photoanode:

NiCoO$_x$/Fe$_2$O$_3$ photoanode was obtained by annealing NiCo(OH)$_x$/Fe$_2$O$_3$ photoanode at 350 °C in air for 2 h. Then, NiCoO$_x$/Fe$_2$O$_3$ photoanode was treated by the same phosphating process, and the as-prepared photoanode was denoted as NiCoP(O)/Fe$_2$O$_3$.

Preparation of NiCoP/Fe$_2$O$_3$ (Air) photoanode:

The as-prepared NiCoP/Fe$_2$O$_3$ photoanode was annealed at 350 °C in air for 10 min, 20 min and 30 min, respectively. Finally, the obtained samples were denoted as NiCoP/Fe$_2$O$_3$ (Air).

Preparation of NiCoP/Fe$_2$O$_3$ (O Plasma) photoanode:

A plasma system (PDC-36G, Hefei Kejing Materials Technology Co., Ltd) was used to treat the surface of NiCoP/Fe$_2$O$_3$ photoanodes at room temperature. The samples were placed on the quartz boat in a plasma reactor. At last, when the chamber pressure was kept at 40 Pa, the samples were treated using O plasma with power of 10.5 W and the treatment time is 10 min, 20 min, 30 min. The obtained samples were denoted as NiCoP/Fe$_2$O$_3$ (O Plasma).

Characterization

The X-ray diffraction spectra (XRD) measurements were performed on a Rigaku RINT-2000 instrument utilizing Cu Kα radiation (40 KV). The XRD patterns were recorded from 10° to 90° with a scanning rate of 0.067°/s. Scanning electron microscopy (SEM) measurements were carried out on a field-emission scanning electron microscope (SU8020. HITACHI) operated at an accelerating voltage of 5 KV. Transmission electron microscopy (TEM) measurements were carried out by using a FEI Tecnai TF20 microscope operated at 200 kV. UV-vis diffuse reflectance spectra were taken on an UV-2550 (Shimadzu) spectrometer by using BaSO$_4$ as the reference. The element composition was detected by X-ray photoelectron spectroscope (XPS, ESCALAB 250Xi). Raman spectroscopy measurements were conducted via a laser Raman microscope system (LabRAM HR Evolution). The exciting laser light wavelength was 532 nm.

Photoelectrochemical measurements.

The Photoelectrochemical properties were measured by an electrochemical analyzer (CHI 760E) in a standard three-electrode system with the as-prepared photoanodes serving as the working electrode, a Pt foil as the counter electrode, and a saturated Ag/AgCl (saturated KCl) as a reference electrode. The illumination source was a 300 W Xe arc lamp (Beijing Perfectlight Technology Co. Ltd., Microsolar 300 UV) equipped with an AM 1.5G filter, and the power intensity of the incident light was calibrated to 100 mW cm^{-2} at the surface of the working electrode. The irradiation area was controlled at 1.0 cm^2. The linear sweep voltammogram (LSV) curves of the electrodes were measured in a voltage window of 0.6-1.6 V$_{RHE}$ with a scan rate of 10 mV/s. A 1 M KOH aqueous solution (pH 13.6) was used as the electrolyte. All potentials of the working electrode were presented against the reversible hydrogen electrode (RHE).

$$E_{RHE} = E_{Ag/AgCl} + E_{Ag/AgCl}\,(reference) + 0.0591 \times pH$$

(E$_{Ag/AgCl}$ (reference) = 0.1976 V vs. NHE at 25 °C)

Where pH is a pH value of the electrolyte.

The IPCE was determined using a motorized monochromator (Oriel Cornerstone 130 1/8 m). IPCE was measured at 1.23 V_{RHE} in 0.1 M KOH aqueous solution (pH 13.6) using the same three-electrode setup described above for photocurrent measurements. IPCE was calculated as follows:

$$IPCE = \frac{1240 \times I(mA/cm^2)}{P_{light}(mW/cm^2) \times \lambda(nm)} \times 100\%$$

Where I is the measured photocurrent density at a specific wavelength, λ is the wavelength of incident light and P_{light} is the measured light power density at that wavelength.

The ABPE was calculated by following equation:

$$ABPE(\%) = \frac{I(mA/cm^2) \times (1.23 - V_{bias})(V)}{P_{light}(mW/cm^2)} \times 100\%$$

Where I is the photocurrent density from the LSV curve shown in Figure 4A, V_{bias} (vs. RHE) is the applied bias, P_{light} is the incident illumination power density (100 mW cm^{-2}).

Mott-Schottky measurements were measured in a 1.0 M KOH aqueous solution at a frequency of 1000 Hz and at a scan rate of 50 mV/s. The potential was measured against an Ag/AgCl reference electrode. The donor concentration is calculated with the following equation:

$$N_d = \frac{2}{e\varepsilon\varepsilon_0}\left[\frac{d(1/C^2)}{dV}\right]^{-1}$$

where N_d is the donor concentration, $e = 1.60 \times 10^{-19}$ C is the electron charge, $\varepsilon = 80$ is the dielectric constant of hematite, $\varepsilon_0 = 8.85 \times 10^{-14}$ F cm^{-1} is the vacuum permittivity, C is the capacitance of the space charge region, and V is the electrode applied potential.

The electrochemical impedance spectroscopy (EIS) Nyquist plots were measured in a 1.0 M KOH aqueous solution at 1.23 V_{RHE} with small AC amplitude of 10 mV in the frequency range of 0.1 to 10^5 Hz under AM 1.5G illumination (100 mW cm^{-2}). The measured spectra were fitted with Z-view software.

Light absorptance of a semiconductor can be calculated using the following equation:

$$\eta_{light} = 1 - 10^{-A}$$

$$A = 1 - Reflectance - Transmittance$$

Reflectance (R) and Transmittance (T) were measured experimentally by UV-vis spectroscopy.

The photocurrent density arising from PEC performance can be described as following:

$$J_{PEC} = J_{abs} \times \eta_{separation} \times \eta_{injection}$$

where J_{abs} is the photocurrent density when completely converting the absorbed photons into current (i.e., absorbed photon-to-current efficiency (APCE) = 100 %). Adding 0.5 M H_2O_2 into the electrolyte (1 M KOH) can largely suppress the surface recombination of charge carriers without influencing the charge separation in the electrode bulk (i.e., $\eta_{injection}$ could be regarded as 100 %). Therefore, $\eta_{separation}$ and $\eta_{injection}$ can be determined as following:

$$\eta_{separation} = J_{H_2O_2}/J_{abs}$$

$$\eta_{injection} = J_{H_2O}/J_{H_2O_2}$$

Where J_{H_2O} and $J_{H_2O_2}$ is the photocurrent density for PEC H_2O oxidation and H_2O_2 oxidation, respectively.

Detection of the amount of hydrogen and oxygen evolution:

To quantitatively determine the amount of H_2 and O_2 produced from the overall water splitting, an online gas analysis system (Labsolar 6A, Beijing Perfectlight Technology Co. Ltd.) and a gas chromatograph (GC 7890A, Agilent Technologies) were employed. The produce of H_2 and O_2 was performed in a three-electrode system at a constant bias of 1.23 V_{RHE} under AM 1.5G illumination (100 mW cm^{-2}).

Electrochemical measurements:

Electrolysis experiments were performed in a standard three-electrode cell, which was composed of working electrode (Fe_2O_3-based photoanodes), counter electrode (Pt foil) and reference electrode (Ag/AgCl, sat. KCl). 1 M KOH was used as the electrolyte. The OER properties were performed from 0 to 2.0 V vs. Ag/AgCl with a scan rate of 5 mV s^{-1}. Electrochemical active surface areas (ECSAs) were measured by cyclic voltammetry (CV) at the potential window -0.33 ~ -0.25 V vs. Ag/AgCl, with different scan rates of 10, 30, 50, 70, 90 and 110 mV s^{-1}. By plotting the $\triangle J = (J_a-J_c)$ at -0.29 V vs. Ag/AgCl against the scan rate, the linear slope which is twice of the double-layer capacitance (C_{dl}) is used to represent ECSAs.
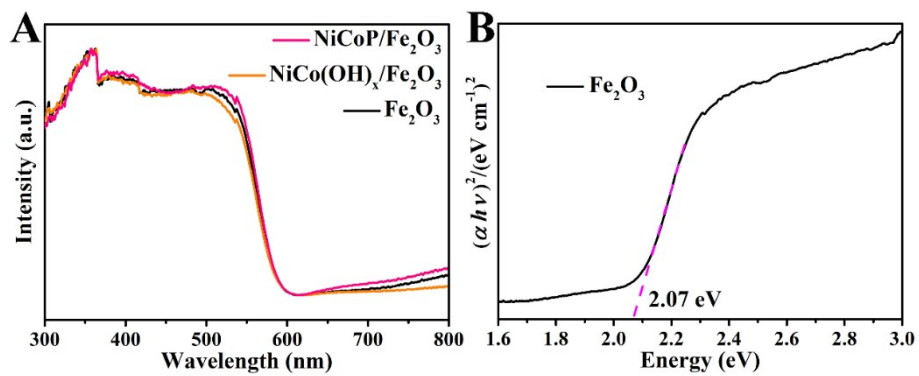
Supplemental Figures and Tables
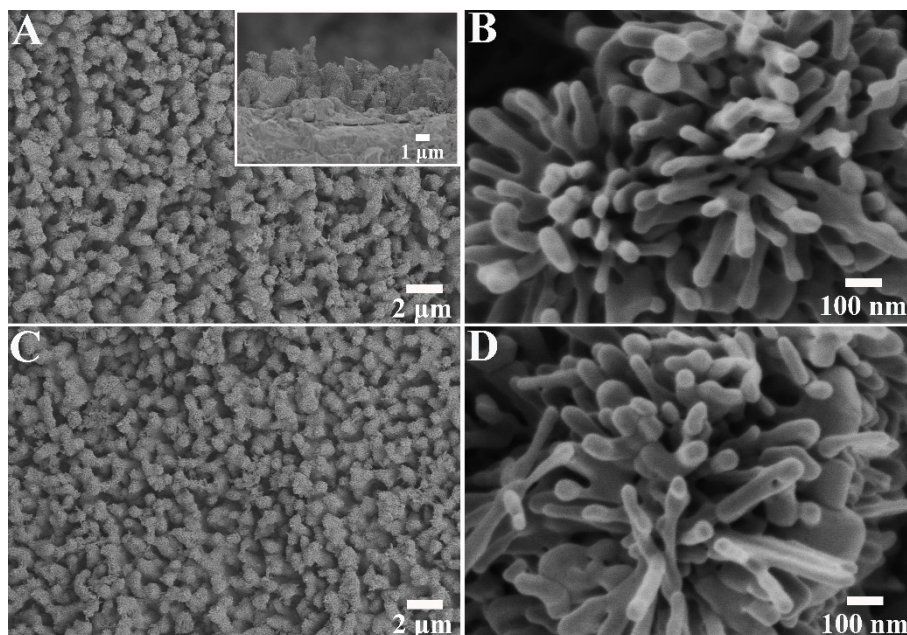
Figure S1. Low and high-resolution SEM images of Fe_2O_3 (A, B) and $NiCo(OH)_x/Fe_2O_3$ (C, D) photoanodes.
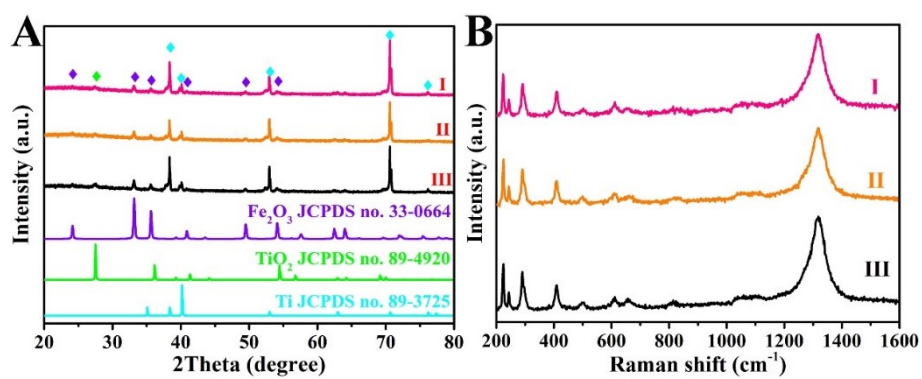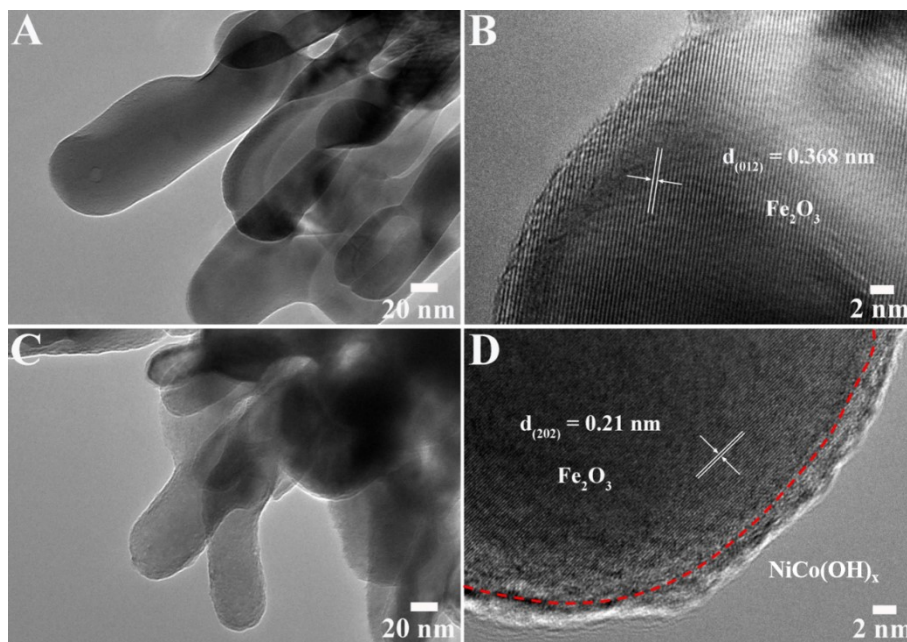

Figure S2. (A) XRD patterns and (B) Raman spectra of Fe_2O_3 (III), $NiCo(OH)_x/Fe_2O_3$ (II) and
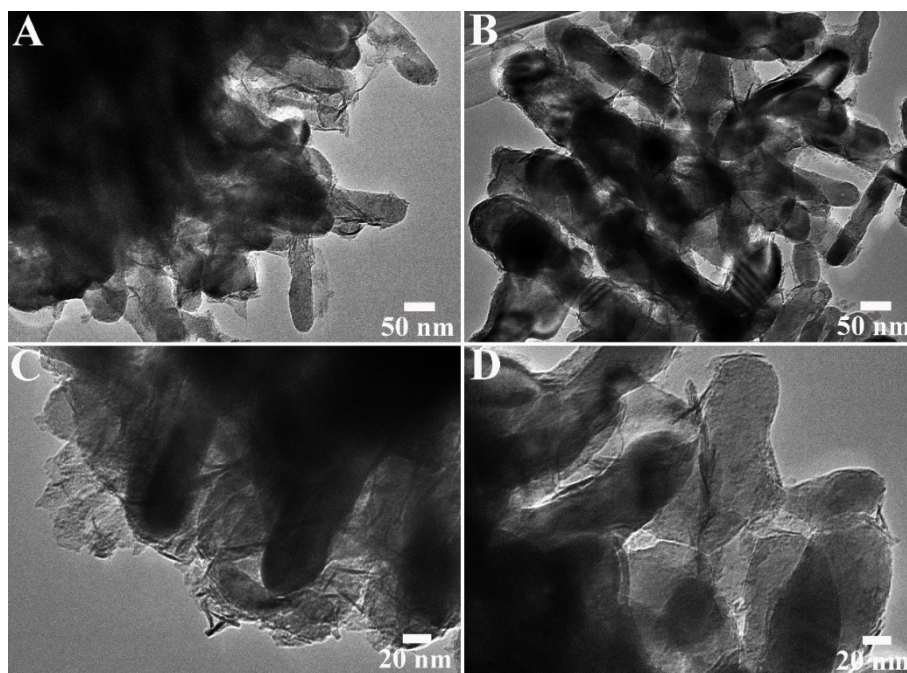
NiCoP/Fe$_2$O$_3$ (I) photoanodes.

Figure S3. (A) UV-vis diffuse reflectance spectra of Fe$_2$O$_3$, NiCo(OH)$_x$/Fe$_2$O$_3$ and NiCoP/Fe$_2$O$_3$ photoanodes. (B) Tauc plots of Fe$_2$O$_3$ photoanodes.

Figure S4. TEM and HRTEM images of Fe$_2$O$_3$ (A, B) and NiCo(OH)$_x$/Fe$_2$O$_3$ (C, D).
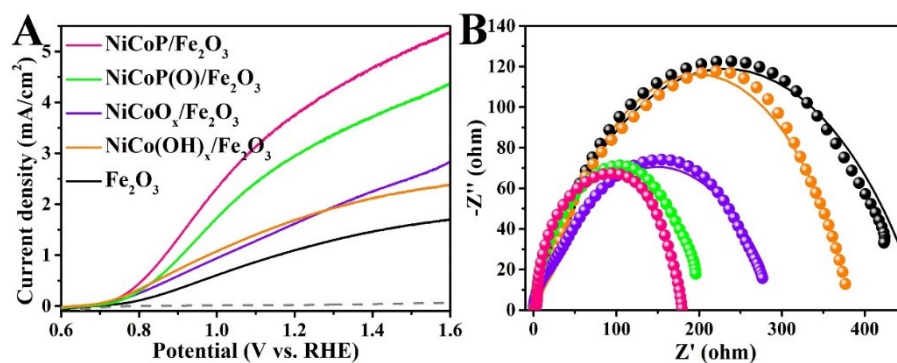
Figure S5. TEM images of NiCoP/Fe$_2$O$_3$.
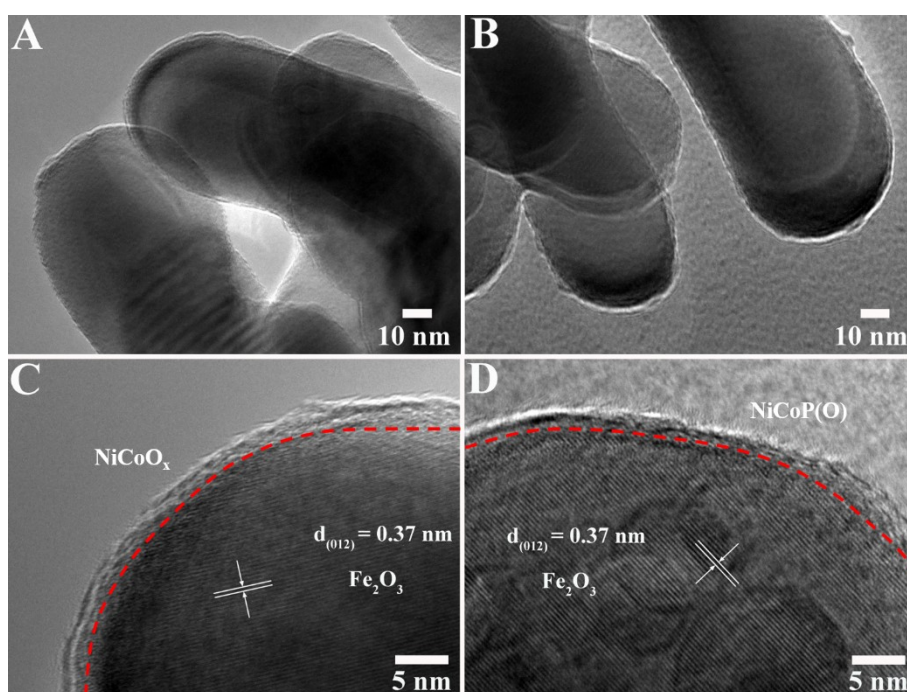
**Figure S6.** TEM and HRTEM images of NiCoO$_x$/Fe$_2$O$_3$ (A, C) and NiCoP(O)/Fe$_2$O$_3$ (B, D).
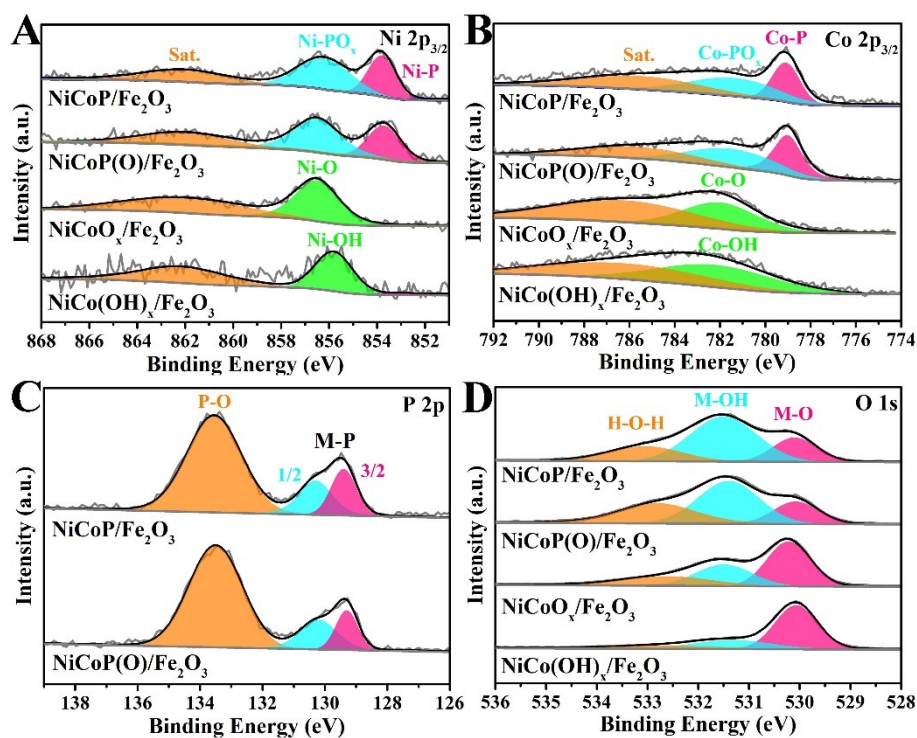
Figure S7. (A) Ni $2p_{3/2}$, (B) Co $2p_{3/2}$, (C) P 2p and (D) O 1s XPS spectra of NiCo(OH)$_x$/Fe$_2$O$_3$, NiCoO$_x$/Fe$_2$O$_3$, NiCoP(O)/Fe$_2$O$_3$ and NiCoP/Fe$_2$O$_3$ photoanodes.

Figure S8. (A) LSV curves and (B) EIS Nyquist plots of pristine Fe$_2$O$_3$, NiCo(OH)$_x$/Fe$_2$O$_3$, NiCoO$_x$/Fe$_2$O$_3$, NiCoP(O)/Fe$_2$O$_3$ and NiCoP/Fe$_2$O$_3$ photoanodes. The EIS curves were measured at 1.23 V_{RHE} in 1 M KOH under AM 1.5G illumination (100 mW cm^{-2}).
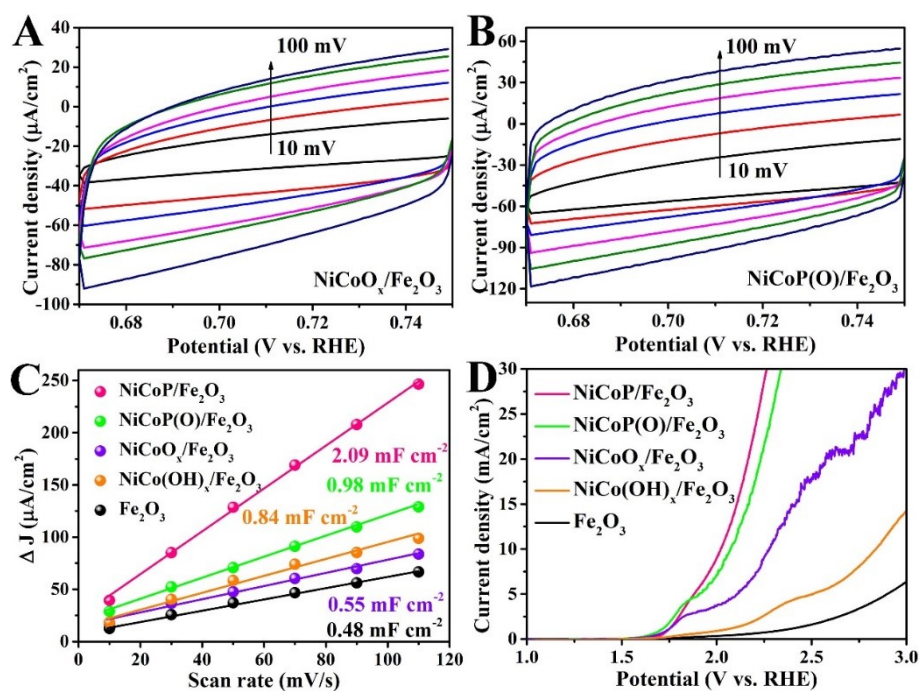
Figure S9. Electrochemical surface area (ESCA) tests towards OER in 1 M KOH. CV curves of $NiCoO_x/Fe_2O_3$ (A), $NiCoP(O)/Fe_2O_3$ (B) with different scanning rates. (C) Difference in current density plotted against the scan rate for the determination of the ECSAs ($2C_{dl}$) and (D) electrochemical OER performance of pristine Fe_2O_3, $NiCo(OH)_x/Fe_2O_3$, $NiCoO_x/Fe_2O_3$, $NiCoP(O)/Fe_2O_3$ and $NiCoP/Fe_2O_3$ photoanodes.

Additional discussion:

To explore the mechanism of the in-situ growth of NiCoP nanosheets, $NiCoO_x/Fe_2O_3$ and $NiCoP(O)/Fe_2O_3$ photoanodes were respectively prepared. As shown in Figure S6A and C, $NiCo(OH)_x$ were transformed to $NiCoO_x$ after annealing in air, and they still retain the nanolayer structure. Similarly, $NiCoO_x$ could be also converted into NiCoP(O) by a phosphorization process. However, the obtained NiCoP(O) is not a nanosheet but a nanolayer (Figure S6B and D). This result indicates that the amorphous structure of $NiCo(OH)_x$ and the loose interfacial contact between $NiCo(OH)_x$ nanolayers and Fe_2O_3 nanorods are favorable to the in-situ growth of NiCoP nanosheets. XPS spectra of the obtained $NiCoO_x/Fe_2O_3$ and $NiCoP(O)/Fe_2O_3$ photoanodes were also performed. The results in Figure S7 could verify the formation of NiCoP(O), and they have the similar chemical states with NiCoP. The PEC performance of $NiCoO_x/Fe_2O_3$ and $NiCoP(O)/Fe_2O_3$ photoanodes were also examined in 1M KOH under AM 1.5 G illumination. As shown in Figure S8, the photocurrent density of $NiCo(OH)_x/Fe_2O_3$ photoanodes have not been

improved after annealing in air, but the resistance of interfacial charge transfer was obviously reduced due to the tight interfacial contact between $NiCoO_x$ nanolayers and Fe_2O_3 nanorods. After phosphating, $NiCoP(O)/Fe_2O_3$ photoanodes also exhibit a significantly enhanced photocurrent density of 3.1 mA cm^{-2}. However, this value is still lower than that of $NiCoP/Fe_2O_3$ photoanodes mainly because of the small surface area of $NiCoP(O)$ nanolayer. To explore the effects of $NiCoO_x$ and $NiCoP(O)$ nanolayer on the PEC water oxidation performance, the relative electrochemical tests were also carried out for $NiCoO_x/Fe_2O_3$ and $NiCoP(O)/Fe_2O_3$ photoanodes. As shown in Figure S9A-C, when $NiCo(OH)_x$ were converted to $NiCoO_x$, the number of surface active sites is reduced because Ni^{3+}/Co^{3+} have a great proportion in $NiCoO_x$ nanolayer (Figure S7A, B). But the $NiCoO_x/Fe_2O_3$ photoanodes show an improved OER activity compared with $NiCo(OH)_x/Fe_2O_3$ photoanodes, which could be attributed to the enhanced charge transfer process. Finally, after phosphating treatment, both ECSAs and OER activity exhibit a remarkable improvement, further clarify that metal phosphides have stronger water oxidation capacity than that of metal oxides and hydroxyl oxides.
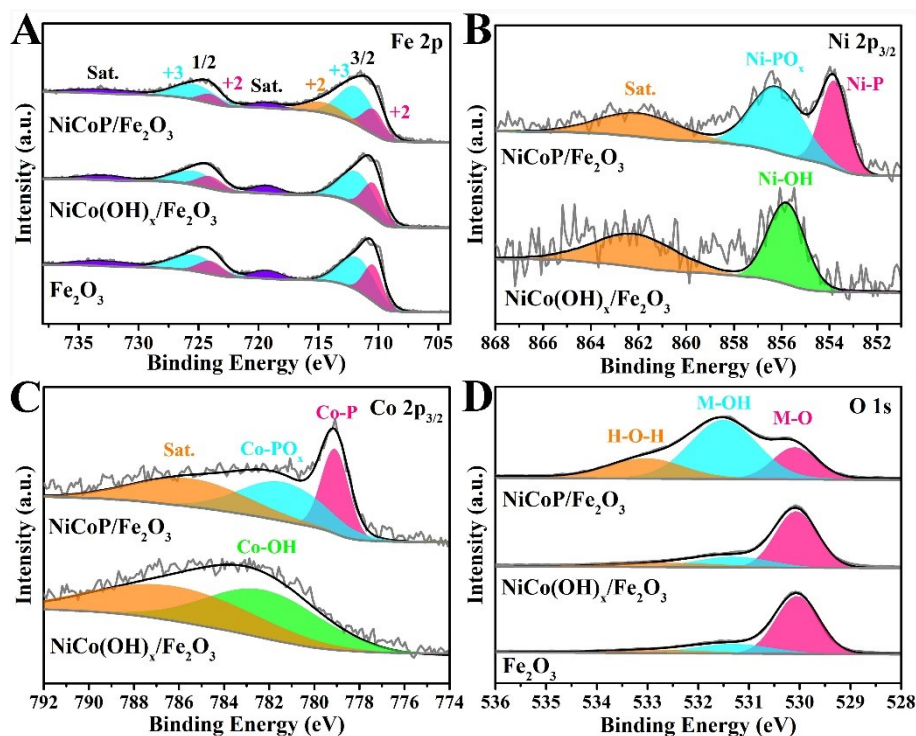
Figure S10. (A) Fe 2p, (B) Ni $2p_{3/2}$, (C) Co $2p_{3/2}$ and (D) O 1s XPS spectra of Fe_2O_3, $NiCo(OH)_x/Fe_2O_3$ and $NiCoP/Fe_2O_3$ photoanodes.
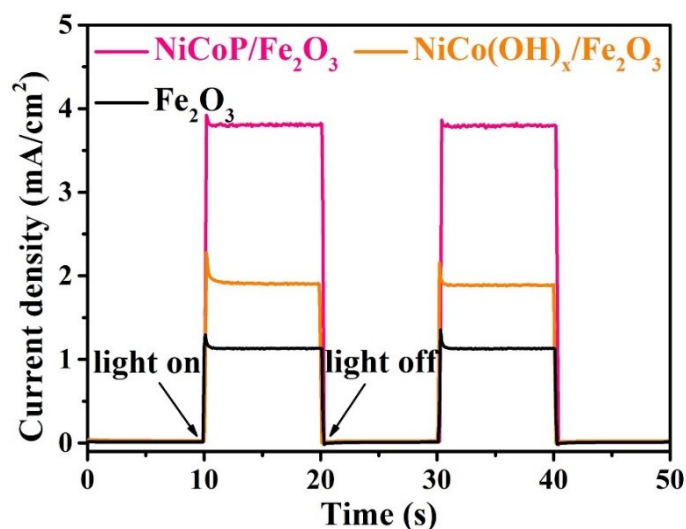
Additional discussion:

In Figure S10D, the O 1s spectra of Fe_2O_3, $NiCo(OH)_x/Fe_2O_3$ and $NiCoP/Fe_2O_3$ photoanodes can be fitted into three peaks located at 530.06, 531.3 and 532.6 eV, respectively corresponding to the lattice oxygen (M-O), oxygen in OH- groups at the surface, physi- and chemisorbed water (H-O-H), respectively.[1-3] However, the OH- and H-O-H peaks of $NiCoP/Fe_2O_3$ photoanode are increased dramatically after phosphorization, revealing that NiCoP cocatalysts possess a stronger adsorption capacity of H_2O and OH-.
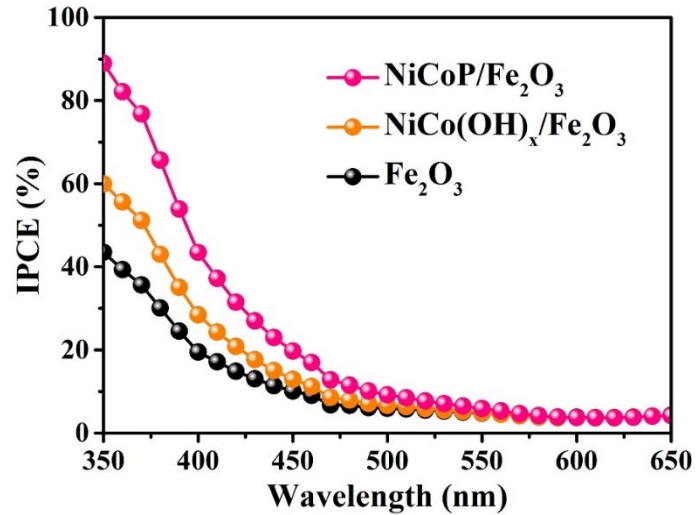
Figure S11. IPCE curves of the pristine Fe_2O_3, $NiCo(OH)_x/Fe_2O_3$ and $NiCoP/Fe_2O_3$ photoanodes. The IPCE curves were measured at 1.23 V_{RHE} in 1 M KOH under AM 1.5G illumination (100 mW/cm^2).
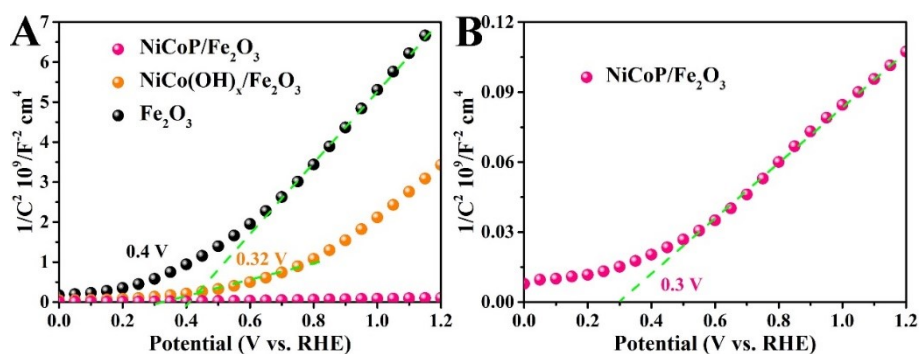
Additional discussion:

The incident photon-to-current conversion efficiency (IPCE) curves were tested at 1.23 V_{RHE} under AM 1.5 G illumination (Figure S11). It can be clearly seen that $NiCoP/Fe_2O_3$ photoanode achieves the maximum IPCE value of 88 % at 350 nm, about 2 times higher than that of the pristine Fe_2O_3 photoanode (42 % at 350 nm). This result indicates that the photoconversion efficiency of photoanodes have been remarkably improved.

Figure S12. Current-time curves of Fe_2O_3, $NiCo(OH)_x/Fe_2O_3$ and $NiCoP/Fe_2O_3$ photoanodes were measured at 1.23 V_{RHE} under chopped illumination.

Additional discussion:

Accordingly, the enhanced PEC performance is related to the reduction of surface charge recombination, which can be further confirmed by the typical current-time curves.[4] In Figure S12, the pristine Fe_2O_3 photoanode shows a strong spike when the light is turned on in each cycle, suggesting severe charge recombination due to its slow water oxidation kinetics. In contrast, the spike is almost vanished after being decorated with ultrathin NiCoP nanosheets, which could be ascribed to the enhanced surface charge separation in $NiCoP/Fe_2O_3$ photoanode.

**Figure S13.** Mott-Schottky plots of pristine Fe_2O_3, $NiCo(OH)_x/Fe_2O_3$ and $NiCoP/Fe_2O_3$ photoanodes.

Additional discussion:

To investigate the impacts of OER cocatalyst modification to the flat-band potential and carrier density, Mott-Schottky curves were conducted in 1 M KOH electrolyte under dark. As shown in Figure S13, all photoanodes exhibit positive slopes, indicating n-type semiconductor feature.[5] Obviously, the flat-band potential of the $NiCo(OH)_x/Fe_2O_3$ and $NiCoP/Fe_2O_3$ photoanodes show a negative shift compared to that of the pristine Fe_2O_3 photoanode, which is consistent with the change of onset potential in LSV curves (Figure 4A), suggesting stronger driving force at the cathode for H_2 evolution.[6] Besides, according to the slopes of Mott-Schottky curves, the carrier density (N_d) of the pristine Fe_2O_3, $NiCo(OH)_x/Fe_2O_3$ and $NiCoP/Fe_2O_3$ photoanodes are 2.03×10^{20} cm^{-3}, 1.04×10^{21} cm^{-3} and 1.6×10^{22} cm^{-3} respectively. The enhancement of N_d leads to better conductivity in the bulk and promotes band bending at the interface of electrode/electrolyte, which facilitates the processes of charge transfer.[7,8]
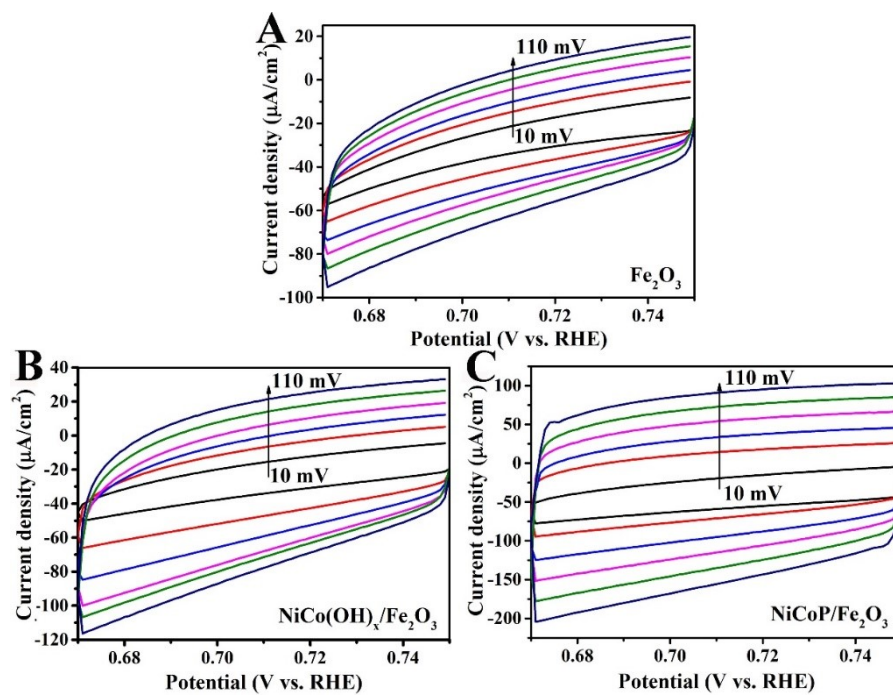
Figure S14. Electrochemical surface area (ESCA) tests towards OER in 1 M KOH. CV curves of Fe$_2$O$_3$ (A), NiCo(OH)$_x$/Fe$_2$O$_3$ (B) and NiCoP/Fe$_2$O$_3$ (C) with different scanning rates.
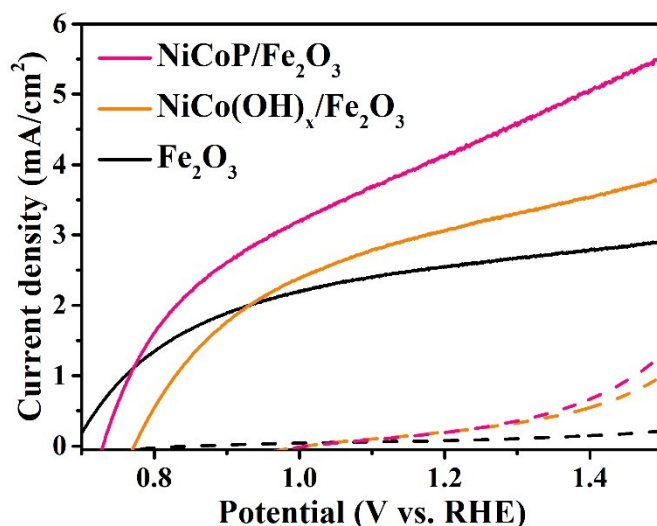
Figure S15. LSV curves of Fe_2O_3, $NiCo(OH)_x/Fe_2O_3$ and $NiCoP/Fe_2O_3$ photoanodes for H_2O_2 oxidation under AM 1.5G illumination (100 mW cm^{-2}, solid line) and dark (dash line).
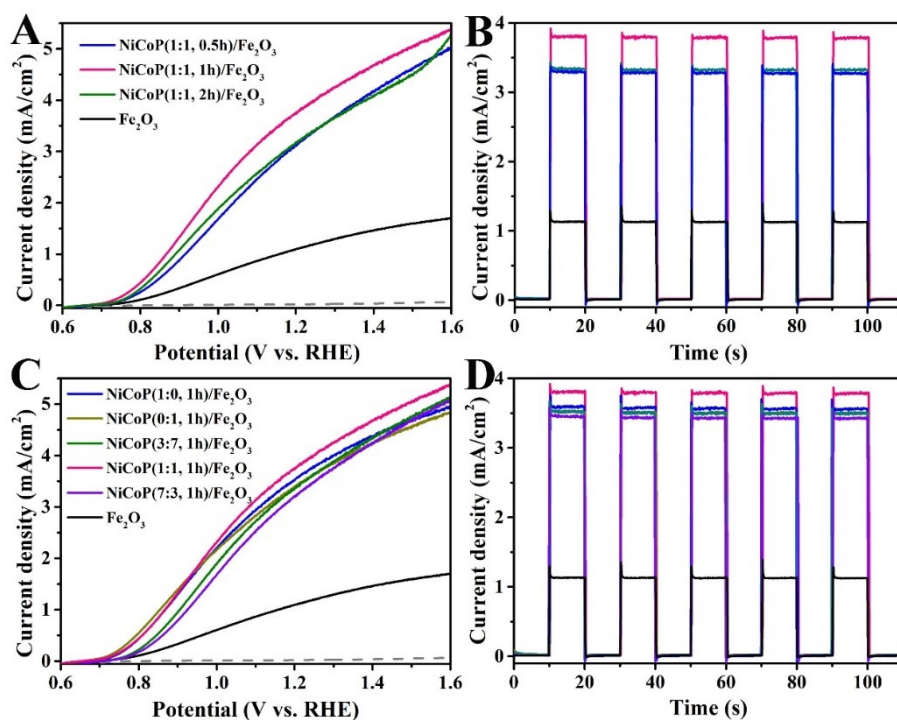
Additional discussion:

The LSV curves of Fe_2O_3, $NiCo(OH)_x/Fe_2O_3$ and $NiCoP/Fe_2O_3$ photoanodes for H_2O_2 oxidation under dark have also been measured in 1M KOH electrolyte (contains 0.5 M H_2O_2). As shown in Figure S15, the current densities of the three samples under dark were all much lower than that under light illumination, confirming that the H_2O_2 oxidation should be mainly attributed to the photo-generated holes. Moreover, it can be observed that $NiCoP/Fe_2O_3$ photoanodes exhibit a higher photocurrent density than both $NiCo(OH)_x/Fe_2O_3$ and Fe_2O_3 photoanodes, revealing that NiCoP cocatalyst could effectively promote the surface injection efficiency of photo-generated holes for H_2O_2 oxidation.

Based on the above results, the produced efficiency of holes could be calculated as follows:

$$\eta = \frac{I_L - I_D}{I_L} \times 100\%$$

Where I_L is the current density for H_2O_2 oxidation under AM 1.5G illumination, I_D is the current density for H_2O_2 oxidation under dark. The hole production efficiency of pristine Fe_2O_3, $NiCo(OH)_x/Fe_2O_3$, and $NiCoP/Fe_2O_3$ photoanodes is 96.8 %, 92.6 % and 94.6 %, respectively, at 1.23 V_{RHE}.

Figure S16. LSV curves and current-time curves of NiCoP/Fe$_2$O$_3$ photoanodes with different immersion times (A, B) and proportion of nickel and cobalt (C, D).

Additional discussion:

By comparing the photocurrent density, optimal impregnation time and Ni/Co ratio can be determined. As shown in Figure S16, NiCoP/Fe$_2$O$_3$ photoanodes with impregnation time of 1 h and the Ni/Co ratio of 1:1 exhibit the highest photocurrent density.
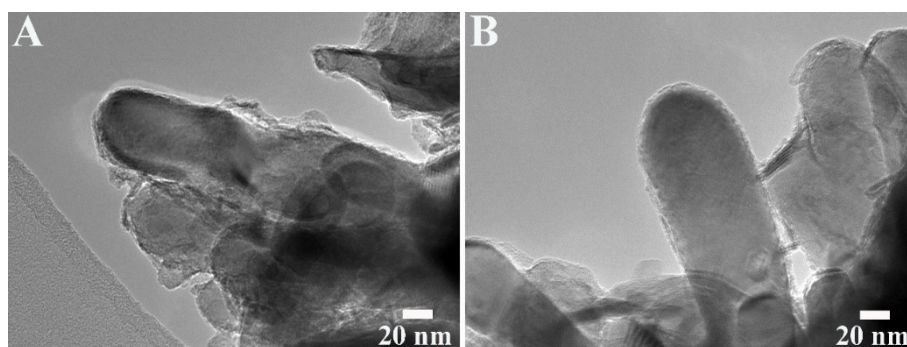
Figure S17. TEM images of NiCoP/Fe$_2$O$_3$ treated by O plasma (A) and annealing in air at 350 °C (B) for 30 min.
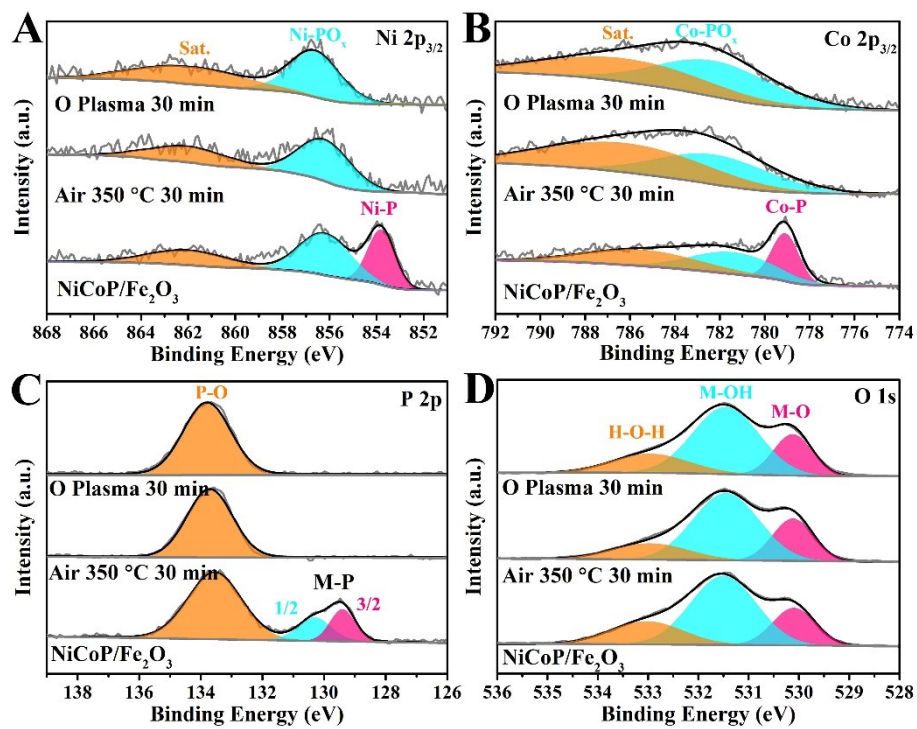
Figure S18. (A) Ni 2p$_{3/2}$, (B) Co 2p$_{3/2}$, (C) P 2p and O 1s XPS spectra of NiCoP/Fe$_2$O$_3$ photoanodes treated by O plasma (A) and annealing in air at 350 °C (B) for 30 min.
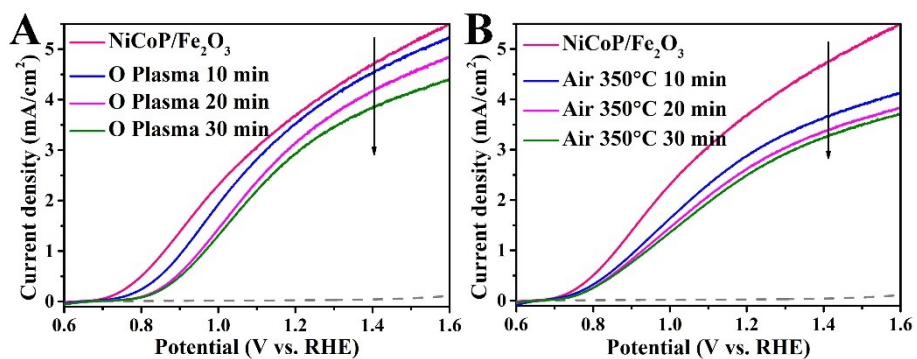
Figure S19. LSV curves of NiCoP/Fe$_2$O$_3$ photoanodes treated by O plasma (A) and annealing in air at 350 °C (B) with different time.
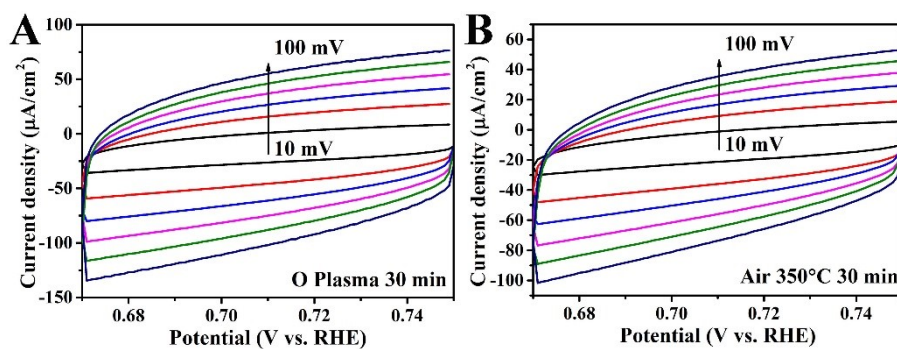
Figure S20. CV curves with different scanning rates of NiCoP/Fe$_2$O$_3$ photoanodes treated by O plasma (A) and annealing in air at 350 °C (B).
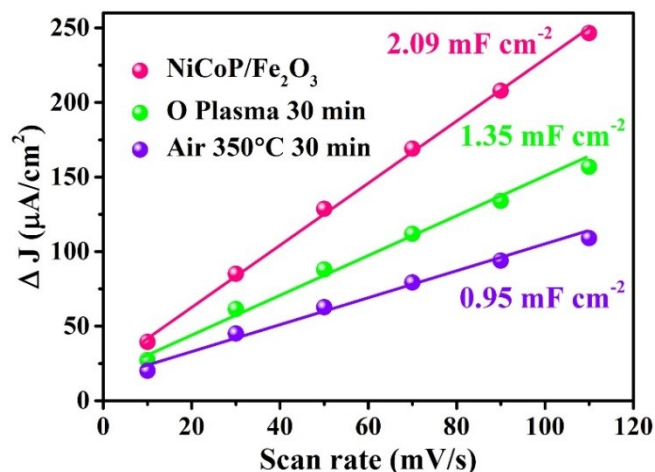
Figure S21. Difference in current density plotted against the scan rate for the determination of the ECSAs ($2C_{dl}$).

Additional discussion:

To prove the key role of metal phosphates on the PEC water oxidation, the obtained $NiCoP/Fe_2O_3$ photoanodes were respectively treated by O plasma and air annealing. Figure S17 shows TEM images of $NiCoP/Fe_2O_3$ photoanodes after O plasma and air annealing treatment. It can be clearly seen that the morphology of two samples have been hardly changed, indicating the tight interfacial contact between Fe_2O_3 nanorods and NiCoP nanosheets. XPS spectra were also conducted to explore the change of chemical states. As shown in Figure S18, both O plasma and air annealing treatment could significantly reduce the proportion of Ni-P and Co-P bonds, which should be attributed to the breaking of M-P bonds and the formation of P-O bonds in NiCoP nanosheets. Besides, in the O 1s spectrum, the peak of H_2O shows an obvious increase after O plasma and air annealing treatment, suggesting that the adsorption capacity of water molecules has been decreased. XPS results proved that both O plasma and air annealing treatment changed the surface chemical states of NiCoP nanosheets. The LSV curves of the treated $NiCoP/Fe_2O_3$ photoanodes were measured under the same condition. As shown in Figure S19, the photocurrent density of $NiCoP/Fe_2O_3$ photoanodes exhibits an obvious decrease along with the extension of treatment time, which should be attributed to the formation of phosphates and the decrease of adsorption energy of water. In addition, the double layer capacitances (C_{dl}) were tested to estimate the effect of O plasma and air annealing on the electrochemically active surface areas (ECSAs). As shown in Figure S21, both O plasma and air annealing treatment significantly reduced the number of active sites, which is also a key reason for the decrease of PEC performance.
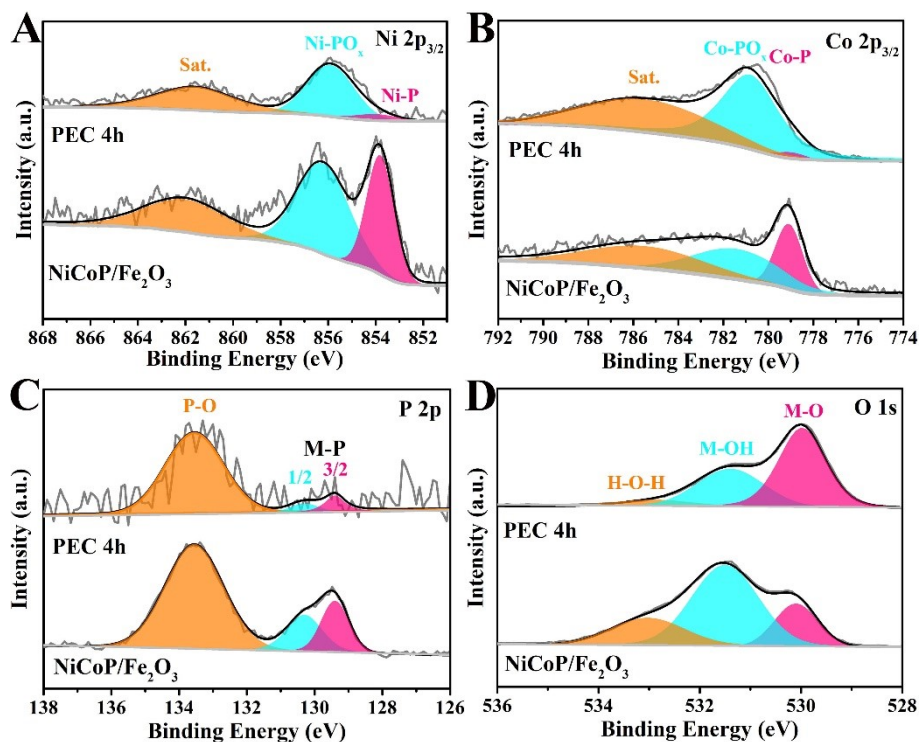
Figure S22. (A) Ni $2p_{3/2}$, (B) Co $2p_{3/2}$, (C) P 2p, (D) O 1s XPS spectra of NiCoP/Fe$_2$O$_3$ photoanode before reaction and after long-term stability measurement.

Additional discussion:

Figure S22 shows the Ni $2p_{3/2}$, Co $2p_{3/2}$, P 2p, and O 1s spectra of the NiCoP/Fe$_2$O$_3$ photoanodes before reaction after long-term stability measurement. The peaks (Ni-P and Co-P bonds) located at the lower binding energy in the Ni $2p_{3/2}$ and Co $2p_{3/2}$ spectra evidently decreased after the long-term stability measurement, indicating the transformation of metal phosphides into metal oxide/oxyhydroxide.[15] Besides, this transformation can be further confirmed by a dramatic decrease of the lower binding energy peaks (M-P bonds) in the P 2p spectra (Figure S22C).[15] Moreover, the height of the M-O peak (Figure S22D) increased dramatically, suggesting the formation of the metal oxide/oxyhydroxide on the surface of NiCoP. Therefore, these results confirmed that the surface of NiCoP/Fe$_2$O$_3$ was enriched with metal oxide/oxyhydroxide during PEC water oxidation reaction, which are known as the OER active phases.[16]

Table S1. Comparison of photocurrent density and ABPE of Fe_2O_3-based photoanodes.

Photoanodes	Photocurrent density (1.23 V_{RHE})	ABPE (%)	Electrolyte	Reference
NiCoP/Fe_2O_3	3.8	0.53	1 M KOH	This work
Co-Pi/Co_3O_4/Ti:Fe_2O_3	2.7	0.43	1 M KOH	4
α-Fe_2O_3-Ni-NC-300	1.85	0.18	1 M NaOH	5
Fe@Ni-MOF/Fe_2O_3:Ti	2.3	0.15	1 M KOH	9
Co-Mn-α-Fe_2O_3	2.09	0.25	1 M NaOH	10
FeP/Ti-Fe_2O_3	3.9	0.33	1 M KOH	11
grad-P:Fe_2O_3/Co-Pi	2.0	0.32	1 M KOH	12
NiO/P-α-Fe_2O_3	2.08	0.23	1 M KOH	13
FeOOH/Fe_2O_3@FeTaO	2.86	0.34	1 M NaOH	14

4

Table S2. The values of the elements in equivalent circuit fitted in the Nyquist plots of Figure. 4E.

Photoanodes	R_s (Ω)	R_{bulk} (Ω)	CPE_{bulk}	R_{ct} (Ω)	CPE_{ct}
Fe_2O_3	1.57	4.44×10^{-9}	5.59×10^{-7}	467.9	2.27×10^{-4}
NiCo(OH)$_x$/Fe_2O_3	1.30	20.32	6.52×10^{-6}	362.5	2.55×10^{-4}
NiCoP/Fe_2O_3	1.18	6.36	4.07×10^{-4}	169.6	6.3×10^{-5}

Reference

[1] J. Xiao, S. Yang, *J. Mater. Chem.,* 2012, **22**, 12253-12262.

[2] J. Yang, H. Liu, W. N. Martens, R. L. Frost, *J. Phys. Chem. C,* 2010, **114**, 111-119.

[3] T. Yoon, K. S. Kim, *Adv. Funct. Mater.,* 2016, **26**, 7386-7393.

[4] S. S. Yi, B. R. Wulan, J. M. Yan, Q. Jiang, *Adv. Funct. Mater.,* 2019, **29,** 1801902.

[5] G. Yang, Y. Li, H. Lin, X. Ren, D. Philo, Q. Wang, Y. He, F. Ichihara, S. Luo, S. Wang, J. Ye, *Small Methods,* 2020, **4**, 2000577.

[6] J. B. Pan, B. H. Wang, J. B. Wang, H. Z. Ding, W. Zhou, X. Liu, J. R. Zhang, S. Shen, J. K. Guo, L. Chen, C. T. Au, L. L. Jiang, S. F. Yin, *Angew. Chem. Int. Ed.,* 2021, **133**, 1453-1460.

[7] S. Feng, T. Wang, B. Liu, C. Hu, L. Li, Z. J. Zhao, J. Gong, *Angew. Chem. Int. Ed.,* 2020, **132**, 2060-2064.

[8] M. Zhong, T. Hisatomi, Y. Kuang, J. Zhao, M. Liu, A. Iwase, Q. Jia, H. Nishiyama, T. Minegishi, M. Nakabayashi, N. Shibata, R. Niishiro, C. Katayama, H. Shibano, M. Katayama, A. Kudo, T. Yamada, K. Domen, *J. Am. Chem. Soc.,* 2015, **137,** 5053-5060.

[9] K. Wang, Y. Liu, K. Kawashima, X. Yang, X. Yin, F. Zhan, M. Liu, X. Qiu, W. Li, C. B. Mullins, J. Li, *Adv. Sci.,* 2020, **7**, 2002563.

[10] G. Yang, Y. Li, H. Pang, K. Chang, J. Ye, *Adv. Funct. Mater.,* 2019, **29**, 1904622.

[11] Q. Bu, S. Li, Q. Wu, Y. Lin, D. Wang, X. Zou, T. Xie, *Catal. Sci. Technol.*, 2019, **9**, 5812-5818.

[12] Z. Luo, C. Li, S. Liu, T. Wang, J. Gong, *Chem. Sci.,* 2017, **8**, 91-100.

[13] F. Li, J. Li, J. Zhang, L. Gao, X. Long, Y. Hu, S. Li, J. Jin, J. Ma, *ChemSusChem,* 2018, **11**, 2156-2164.

[14] H. Zhang, W. Y. Noh, F. Li, J. H. Kim, H. Y. Jeong, J. S. Lee, *Adv. Funct. Mater.,* 2019, **29,** 1805737.

[15] H. Liang, A. N. Gandi, D. H. Anjum, X. Wang, U. Schwingenschlogl, H. N. Alshareef, *Nano Lett.* 2016, **16**, 7718.

[16] B. You, N. Jiang, M. Sheng, M. W. Bhushan, Y. Sun, *ACS Catal.* 2016, **6**, 714.